


Accepted: 12 September 2018

# A computational strategy for damage-tolerant design of hollow shafts under mixed-mode loading condition

Marcello Antonio Lepore<sup>1</sup> | Rustam Yarullin<sup>2</sup> | Angelo Rosario Maligno<sup>3</sup> | Raffaele Sepe<sup>4</sup> 

<sup>1</sup>Department of Industrial Engineering, University of Salerno, Via G. Paolo II, 132-84084 Fisciano, Italy

<sup>2</sup>Kazan Scientific Center of Russian Academy of Sciences, Lobachevsky Street, 2/31-420111 Kazan, Russia

<sup>3</sup>Institute for Innovation in Sustainable Engineering, University of Derby, Derby, UK

<sup>4</sup>Department of Chemical, Materials and Production Engineering, University of Naples Federico II, P.le V. Tecchio 80, 80125 Naples, Italy

## Correspondence

R. Sepe, Department of Chemical, Materials and Production Engineering, University of Naples Federico II, P.le V. Tecchio 80, 80125 Naples, Italy.  
Email: raffsepe@unina.it

## Abstract

Three-dimensional numerical analyses, using the finite element method (FEM), have been adopted to simulate fatigue crack propagation in a hollow cylindrical specimen, under pure axial or combined axial-torsion loading conditions. Specimens, made of Al alloys B95AT and D16T, have been experimentally tested under pure axial load and combined in-phase constant amplitude axial and torsional loadings. The stress intensity factors (SIFs) have been calculated, according to the J-integral approach, along the front of a part through crack, initiated in correspondence of the outer surface of a hollow cylindrical specimen. The crack path is evaluated by using the maximum energy release rate (MERR) criterion, whereas the Paris law is used to calculate crack growth rates. A numerical and experimental comparison of the results is presented, showing a good agreement in terms of crack growth rates and paths.

## KEYWORDS

crack propagation, finite element method, mixed-mode fracture, multiaxial fatigue

## 1 | INTRODUCTION

Traditionally, steel alloys have been used for shafts in engines, but recently, the advent of stringent requirements in terms of corrosion resistance, high fatigue life, and lightweight has favoured the application of aluminium alloy as an alternative to steel. However, aluminium alloys are more sensitive to fatigue crack growth than steel alloys; therefore, damage tolerance analyses become of the uttermost importance. Structural components, such

as hollow shafts, aeroengine shafts, wind-turbine shafts, and aircraft/helicopter structures, can be subjected to multiaxial fatigue, and the presence of notches can facilitate the onset of fatigue cracks. Consequently, for the shaft failure assessment, the estimation of the critical crack length at which a crack becomes unstable with corresponding prediction of fatigue life is mandatory. Fatigue crack growth analysis of surface flaws is quite complex. The crack front has to be modelled, and the aspect ratio of the crack shape continuously changes during fatigue

**Nomenclature:**  $a$ , crack depth;  $a_0$ , initial crack depth;  $b$ , crack advance measured at break through points;  $\Delta b$ , increment of crack advance measured at break through points;  $c$ , semi chord length;  $c_0$ , initial semi chord length;  $h$ , depth of the initial curvilinear edge notch;  $C$ ,  $m$ , Paris equation constants;  $D$ , specimen external diameter;  $E$ , Young modulus;  $G$ , shear modulus;  $J$ , J-integral;  $K_I$ ,  $K_{II}$ ,  $K_{III}$ , Mode I, II, and III stress intensity factors;  $K_{eff}$ , effective stress intensity factor;  $\Delta K_{eff}$ , effective stress intensity factor range;  $M_t$ , torsion load;  $N$ , number of cycles;  $N_f$ , number of cycles to failure;  $P$ , axial load;  $R$ , cyclic stress ratio;  $\nu$ , Poisson ratio;  $\sigma_{0.2}$ , monotonic tensile yield strength;  $\delta$ , final elongation;  $\psi$ , final reduction of area;  $\sigma_u$ , nominal ultimate tensile strength;  $\sigma_s$ , true ultimate tensile strength;  $n$ , strain hardening exponent;  $\alpha$ , strain hardening coefficient;  $\varphi$ , load phase angle;  $\lambda$ , biaxiality ratio  $\tau_{max}/\sigma_{max}$ ;  $\sigma_{max}$ , nominal maximum axial stress;  $\tau_{max}$ , nominal maximum torsion stress;  $db/dN$ , growth rate at break through points;  $da/dN$ , growth rate in the depth direction;  $a/c$ , aspect ratio;  $a_0/c_0$ , initial aspect ratio;  $a/D$ , relative crack depth;  $b/D$ , relative surface crack chord length; COD, crack opening displacement; CTOD, crack tip opening displacement; DBE, dual boundary element; EDM, electrical discharge machining; FEM, finite element method; MERR, maximum energy release rate; PSM, peak stress method; SED, strain energy density; SIF, stress intensity factor

loading. Usually, part-through flaws start in correspondence of the free surfaces of cylinders and keeps, during the evolution, a quasielliptical<sup>1</sup> shape. Analytical calculations are suitable to predict whether a crack will grow in simple cases, but in complex cases, it is necessary to perform detailed, 3D numerical simulations.

Some studies have been made concerning the prediction of the structural integrity of such cylindrical metallic components; they can be performed through fatigue growth numerical analysis, assuming initial and accumulated in service damages.<sup>2,3</sup>

The finite element (FE) in combination with the dual boundary element (DBE) methods represents a viable option to implement a global-local approach useful to investigate the fatigue behaviour of complex structural components undergoing complex loading conditions within acceptable computational time. In Citarella et al,<sup>4</sup> Giannella et al,<sup>5</sup> Citarella et al,<sup>6</sup> Citarella et al,<sup>7</sup> and Fellingner et al,<sup>4,8</sup> the synergetic combined usage of FEM and DBEM approaches when tackling crack growth problems under mixed mode conditions is shown.

Carpinteri et al<sup>9,10</sup> investigated a hollow metal cylinder affected by a circumferential elliptical surface crack under different loading conditions, such as the bending moment and the axial loading, through numerical models based on 3D FEs.

Predan et al<sup>11</sup> estimated, by means of the FE method, the stress intensity factors (SIFs) for circumferential semielliptical surface cracks involving the cross section of a hollow cylinder under torsion.

Citarella et al<sup>12-16</sup> investigated the crack propagation in hollow shafts under torsion loading and combined axial-torsion loading conditions using both DBE and FE methods.

Shahani and Habibi<sup>17</sup> carried out a study on the mixed-mode fracture induced by a semielliptical circumferential surface crack lying on the external surface of a hollow cylinder cross section; SIFs were numerically calculated through a FE model consisting of hexahedral 20 node-isoparametric elements and a singular form of these FEs at the crack's front.

The ever-increasing automatic remeshing capabilities of specialised FEM software<sup>18-21</sup> have greatly contributed to understand the behaviour of cracked aeroengine shafts undergoing mixed-mode fatigue loading, but some difficulties arise when trying to simulate extended nonplanar crack propagation. Also, the impossibility to model automatically the breakthrough in the hollow shaft requires the development of user-defined crack profiles to apply a "breakthrough" strategy.

In this paper, a computational strategy for damage-tolerant design of hollow shafts under multiaxial loading has been presented which allows efficient and automatic simulation of nonplanar 3D crack propagations.

In particular in this work, experimental tests and three-dimensional crack propagation simulation by FEM have been carried out on a hollow cylinder made in B95AT and D16T aluminium alloy undergoing pure axial and combined axial-torsion loading conditions. Experimental tests have been carried out to obtain realistic data on the crack propagation: The samples have been tested under in-phase constant amplitude axial and torsional loading conditions.

SIFs along the front of an initial part through crack, started from the outer surface of the hollow cylinder, are calculated via the J-integral approach rather than crack tip opening displacement (CTOD), being the former more accurate and less dependent on mesh refinement level.<sup>13,22</sup>

The crack path assessment is performed by using the maximum energy release rate criterion<sup>13,22</sup> whilst the crack growth rates are calculated by the Paris law, calibrated for the material under analysis.

The comparison between the predicted and experimental results showed a good agreement in terms of crack growth rates and paths.

The added value of the proposed work comes from the benchmarking between different software,<sup>16,23</sup> in terms of accuracy (by counter comparison vs experimental results) in predicting the correct values of crack path and crack growth rates, and in terms of runtimes.

## 2 | MATERIALS AND EXPERIMENTAL SET-UP

Dimensions and geometry of a hollow cylindrical specimen are shown in Figure 1; in particular, the diameters  $D$  and  $d$  of gage sections are equal to 28 and 10 mm, respectively. Two types of specimens are considered: one with a circular notch and the other with an elliptical notch. The surface edge notches were cut by electrical discharge machining (EDM), with initial depth  $h = 3.0$  mm for both circular and elliptical shapes; the sizes of each type of notch are reported in Table 1. The crack front can be approximated by an elliptical curve with characteristic sizes  $c$  and  $a$ , where  $c$  is the semichord length and  $a$  is the crack depth.

The size  $b$  is defined as the length, measured along the free surface, of the arc between the advancing crack breakthrough point and the (initial) notch break through point. Two types of fatigue tests were carried out:

- Axial load fatigue tests on specimens with circular and elliptical notch.
- Combined axial/torsion tests on specimens with elliptical notch.

The fatigue tests were carried out under load control, with a frequency of 10 Hz, at room temperature and with

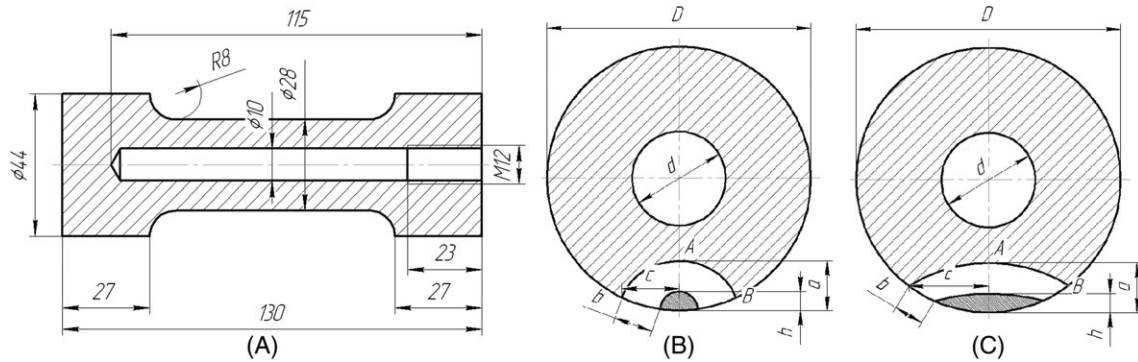


**FIGURE 1** Details of the hollow specimen: dimension and geometry A, initial circular notch B, and initial elliptical notch C

**TABLE 1** Geometrical parameters of notches

Type of Notch	$d$ , mm	$D$ , mm	$h$ , mm	$a_0$ , mm	$c_0$ , mm	$a_0/c_0$
Circular	10	28	3	3	3.3	0.9
Elliptical	10	28	3	3	8.11	0.37

stress ratio  $R = 0.1$ , by means of a multiaxial testing machine (Figure 2). The testing machine is equipped with an axial torsional load cell having an axial and a torsional full scale of 100 and 2.0 kN m, respectively. All specimens were tested applying an only one load level, and the failure criterion was the total failure/rupture of the specimens.

Axial load fatigue tests were carried out applying a maximum nominal load equal to  $P = 35$  kN, whereas combined fatigue tests were performed applying in-phase



**FIGURE 2** Multiaxial testing machine [Colour figure can be viewed at [wileyonlinelibrary.com](http://wileyonlinelibrary.com)]

and synchronous axial and torsion loads, with maximum values equal to  $P = 40$  kN and  $M_t = 250$  N m and biaxiality ratio  $\lambda = \tau_{max}/\sigma_{max} = 0.8$ .

During test, the stress ratio was modified from  $R = 0.1$  to  $R = 0.5$  for a few cycles in order to create beach marks on the fracture surface (Figures 3 and 4) that could be detected in a post mortem fractographic analysis; such stress ratio variation was modified for a number of cycles that produce an increment of surface crack arc length equal to  $\Delta b \cong 0.1$  mm, and it was iteratively applied each time the surface crack arc length increased of  $\Delta b = 1.75 / 2$  mm.

In order to measure the crack arc length  $b$  on the free surface, an optical zoom microscope was used, whereas to measure the crack opening displacement, a COD gauge was applied on the specimen cylindrical surface, in correspondence of the symmetry plane.

The sample materials are aluminium alloys D16T (Al 2024) and B95AT (Al 7075). The mechanical properties are reported in Table 2, where:  $\sigma_{02}$  is the tensile yield strength,  $\sigma_u$  is the ultimate tensile strength,  $\sigma_t$  is the true tensile strength,  $\psi$  is the final percentage area reduction,  $\delta$  is the percentage final elongation,  $E$  is the Young modulus,  $n$  is the strain hardening exponent, and  $\alpha$  is the strain hardening coefficient.

### 3 | EXPERIMENTAL RESULTS

The results of tests are summarised in Table 3. In particular, the applied loads, the values of the nominal

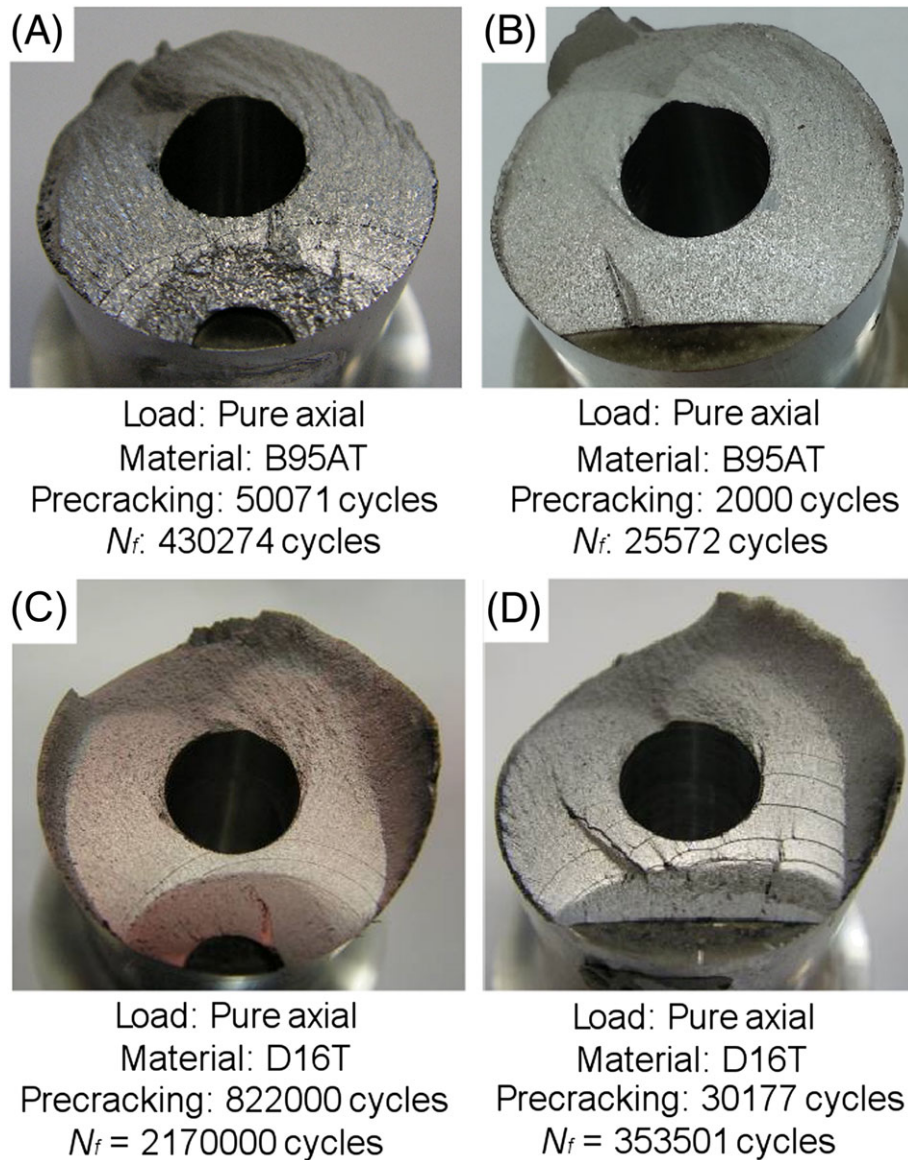


**FIGURE 3** Post mortem cross sections of specimens undergoing pure axial load: circular notch B95AT alloy A, semielliptical notch B95AT alloy B, circular notch D16T alloy C, and semielliptical notch D16T alloy D, [Colour figure can be viewed at [wileyonlinelibrary.com](http://wileyonlinelibrary.com)]

maximum stress, and the number of cycles to failure are reported.

The typical fracture surfaces of different specimens are shown in Figures 3 and 4 both for axial and axial-torsion loadings, respectively.

The crack growth rates were recorded using a zoom optical microscope and COD gauges. The crack front shape and then the parameters  $a$  and  $c$  were obtained by metallographic post mortem analyses, as provided by the beach marks obtained by the previously mentioned periodic stress ratio change. In particular, using a comparison microscope, it was possible to obtain the relations between the dimensionless geometry parameters  $a/c$  and  $a/D$ . In addition, the curve of surface crack

propagation  $b$  versus cycle number  $N$  can be obtained (Figure 5).

Figure 5A shows plots of the curvilinear abscissa  $b$  against the number of cycles  $N$ , for axial fatigue tests on specimens with a circular or an elliptical notch. Figure 5B shows the same parameter with reference to combined axial-torsion tests, carried out on specimens with an elliptical notch (in this case, no samples with circular notch were considered).

As shown in Figure 5A (axial load), the crack growth rates for the specimens (with circular and elliptical notch) made of B95AT are higher than those related to specimens made of D16T. As a matter of fact, considering an initial value of  $b = 1.15$  mm for the circular notch, the

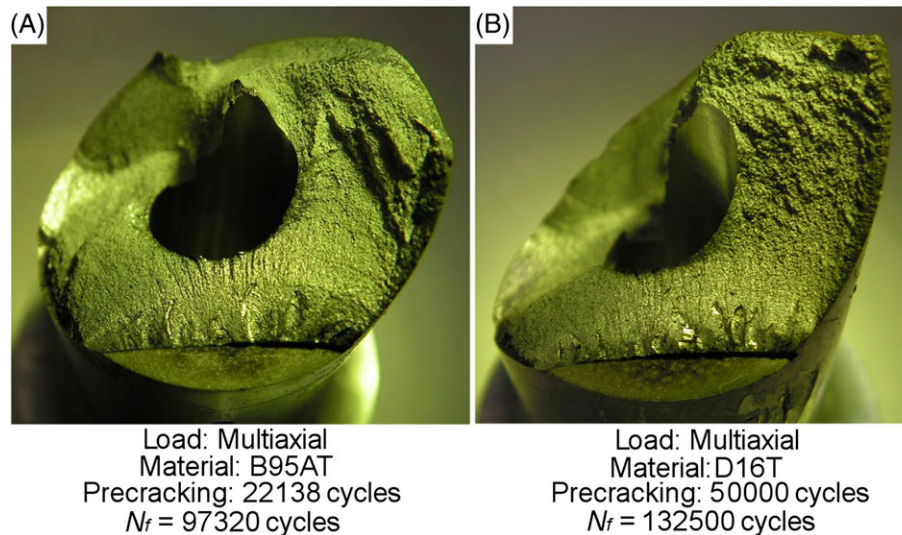


**FIGURE 4** Crack surface of specimens undergoing axial/torsion combined load: B95AT alloy A, and D16T alloy B, [Colour figure can be viewed at [wileyonlinelibrary.com](http://wileyonlinelibrary.com)]

**TABLE 2** Mechanical properties of aluminium alloys at 20°C

Aluminium Alloy	$\sigma_{0.2}$ , MPa	$\sigma_u$ , MPa	$\sigma_b$ , MPa	$\psi$ , %	$\delta$ , %	$E$ , MPa	$n$	$\alpha$
D16T	438	594	665	11	11	76557	5.86	1.54
B95AT	520	586	775	36	14	75274	10.37	1.44

**TABLE 3** Results of fatigue tests

Number of Specimens	Material	Type of Notch	Load Type	$\sigma_{max}$ , MPa	$\tau_{max}$ , MPa	Cycles to Failure
1	B95AT	Circular	Axial $R = 0.1$	65	0	430 274
1	B95AT	Elliptical	Axial $R = 0.1$	65	0	25 572
1	D16T	Circular	Axial $R = 0.1$	65	0	2 170 000
1	D16T	Elliptical	Axial $R = 0.1$	65	0	353 501
1	B95AT	Elliptical	Axial/torsion $R = 0.1, \varphi = 0, \lambda = 0.8$	75	60	97 320
1	D16T	Elliptical	Axial/torsion $R = 0.1, \varphi = 0, \lambda = 0.8$	75	60	132 500

number of cycles to failure are equal to 380 203 and 810 000 for B95AT and D16T alloy, respectively, whereas considering an initial value of  $b = 2$  mm for the elliptical notch, the number of cycles to failure is equal to 23 572 and 84 902 for B95AT and D16T alloy, respectively.

In the case of elliptical notch, in-phase torsion loading superimposed to axial loading leads to an increase of crack growth rates for D16T and to a decrease for B95AT specimens (Figure 5B). As a matter of fact, considering an initial value of  $b = 2$  mm for B95AT and of 0.5 mm for D16T, the number of cycles to failure for

B95AT is equal to 23 288 and 65 373 for axial and axial/torsion loading, respectively, whereas the number of cycles to failure for D16T is equal to 84 902 and 27 500 for axial and axial/torsion loading, respectively. These results are relevant because they highlight that different materials exhibit opposite behaviour when torsional loading is superimposed to axial loading.

The relationship between the arc crack length  $b$  and COD with reference to the specimens undergoing pure axial load and combined axial/torsion loading is shown in Figure 6. It is found that the arc crack length  $b$  can be

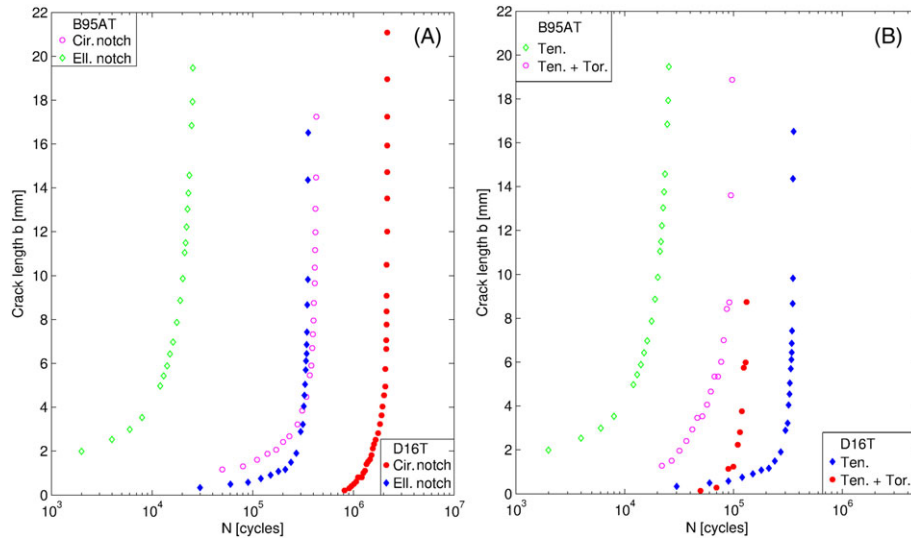
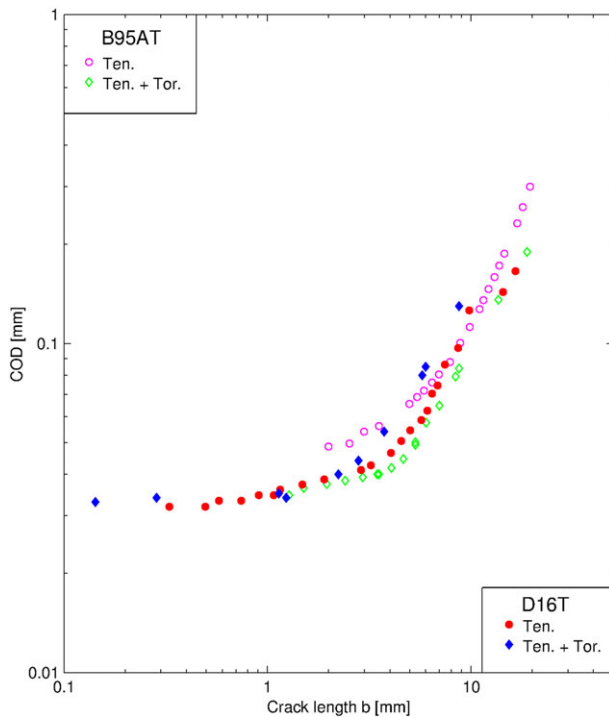


**FIGURE 5** Graphs of arc crack length  $b$  vs cycles: under axial load with circular and elliptical notches A, and under axial or combined axial/torsion loading with elliptical notch B, [Colour figure can be viewed at [wileyonlinelibrary.com](#)]

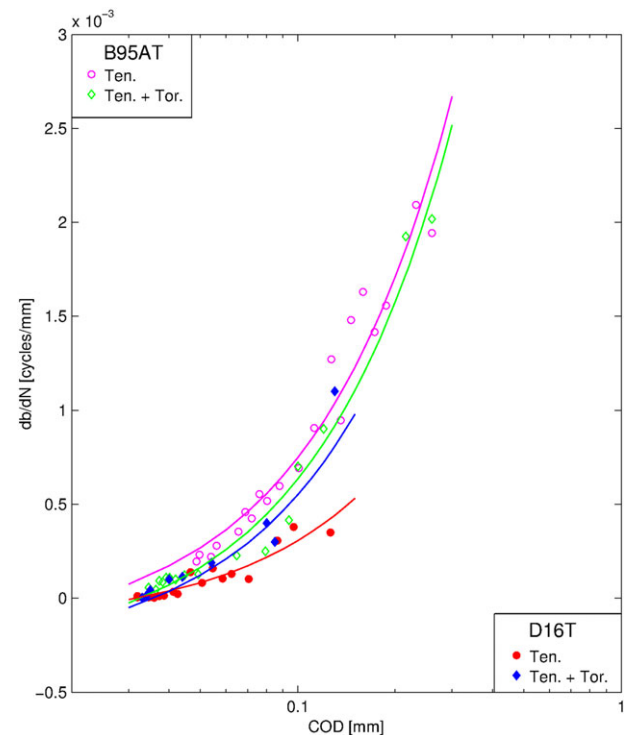
correlated with  $COD$  for all the types of loadings and materials, using a unique fitting curve with a small scatter. This fact suggests the possibility of indirect crack length assessment from  $COD$  experimental measurements, at least in a first approximation.

Figure 7 shows the crack growth rate  $db/dN$  versus  $COD$ , or (indirectly) vs  $b$  (due to the previously demonstrated correlation between  $b$  and  $COD$ ), in the case of

pure cyclic axial and combined axial/torsion fatigue loading. In particular, it is found that for elliptical notches and different load cases and materials, the experimental crack growth rates  $db/dN$  as a function of  $COD$  fit into four curves, whose relative position is consistent with the relative position of curves in Figure 5B. It is interesting to observe the opposite impact of an added torsional



**FIGURE 6**  $COD$  vs arc crack length  $b$  curve [Colour figure can be viewed at [wileyonlinelibrary.com](#)]



**FIGURE 7** Crack growth rate  $db/dN$  vs  $COD$  under different loading conditions for specimen with elliptical notch [Colour figure can be viewed at [wileyonlinelibrary.com](#)]

load on crack growth rates along the external surface: For D16T and B95AT, an acceleration rather than a small slowing down is, respectively, produced.

#### 4 | NUMERICAL ANALYSES

A crack propagation simulation was just performed with reference to a D16T hollow cylindrical specimen with elliptical notch (Figure 1C). The loading conditions of pure axial fatigue and combined axial/torsion fatigue were simulated.

A linear elastic fracture mechanic approach was used for these simulations. The numerical studies were based on FE analyses using the adaptive remeshing approach.

In this study, the commercial software ZENCRACK<sup>24,25</sup> has been adopted for automated 3D remeshing and crack propagation calculations along with ABAQUS<sup>26</sup> as FE solver. The strategy used in this study is described in Citarella et al<sup>14</sup> and Maligno et al<sup>25</sup>

The uncracked model (Figure 8A) consists of 209 020 elements and 226 151 nodes; 209 016 elements are hexahedral 8-node elements of type C3D8, and 4 are hexahedral 20-node elements of type C3D20 both with full integration (such elements define the volume portion that will be remeshed following the crack introduction). The updated FEM model, with crack introduction, is shown in Figure 8B: The elements replacing the four aforementioned C3D20 elements are again hexahedral 20-node elements of type C3D20 with full integration (even if the

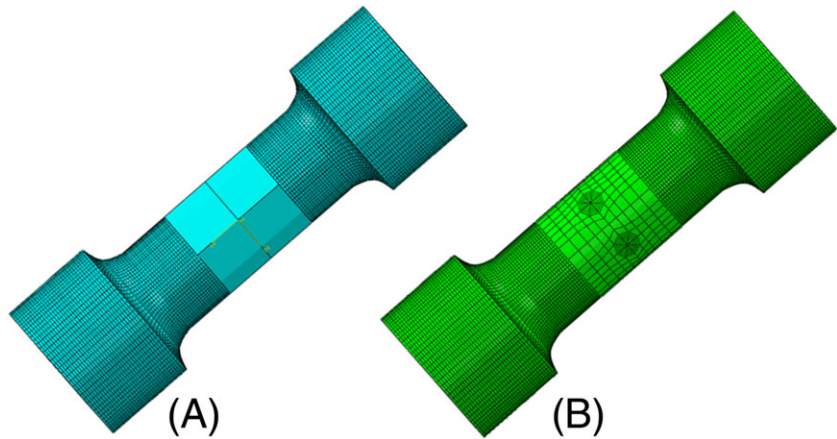


**FIGURE 8** Uncracked model A, and cracked model B, [Colour figure can be viewed at [wileyonlinelibrary.com](http://wileyonlinelibrary.com)]

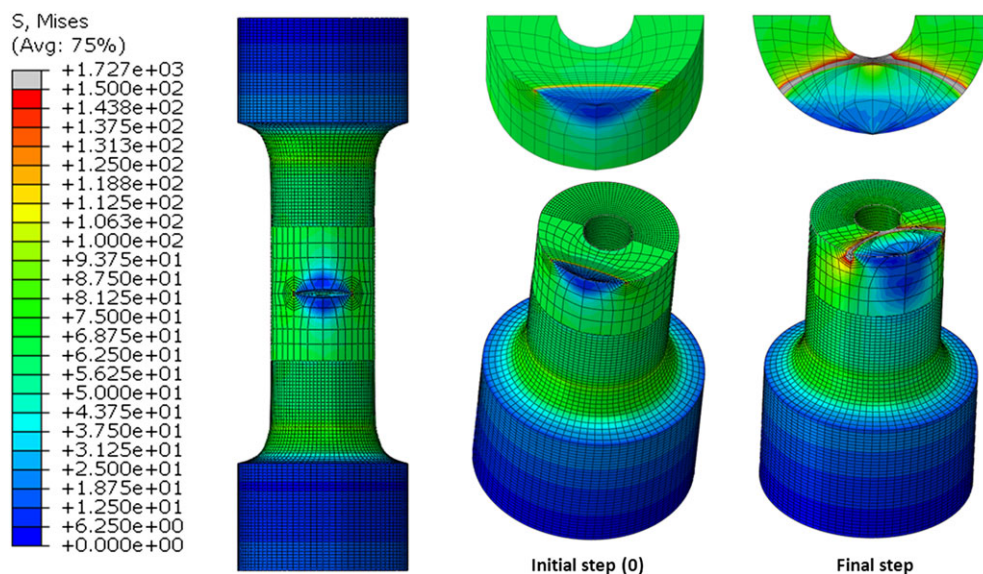


**FIGURE 9** von Mises stress scenario (MPa) for elliptical notch under pure axial load at different step of crack propagation [Colour figure can be viewed at [wileyonlinelibrary.com](http://wileyonlinelibrary.com)]

mesh refinement is lower in the area surrounding the crack, it is based on higher order interpolation elements).

The Paris law has been adopted to calculate the crack growth rate. The Paris law is given by the following relationship:

$$\frac{da}{dN} = C \cdot \Delta K_{eff}^m, \quad (1)$$

where the material constants are  $C = 2.43416e-13 \text{ MPa mm}^{0.5}$ ,  $m = 3.325$  (calibrated by in house made

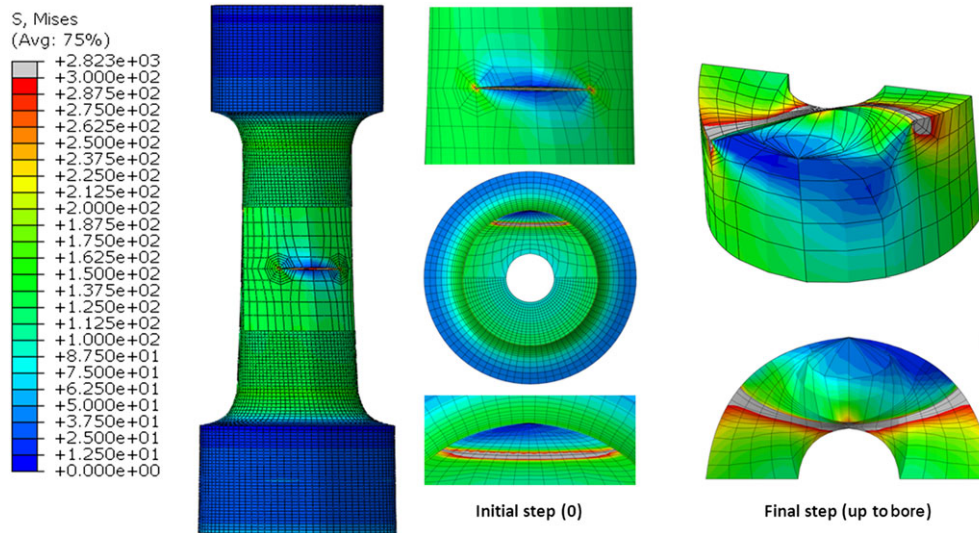


**FIGURE 10** von Mises stress scenario (MPa) for elliptical notch under axial/torsion loading at different step of crack propagation [Colour figure can be viewed at wileyonlinelibrary.com]

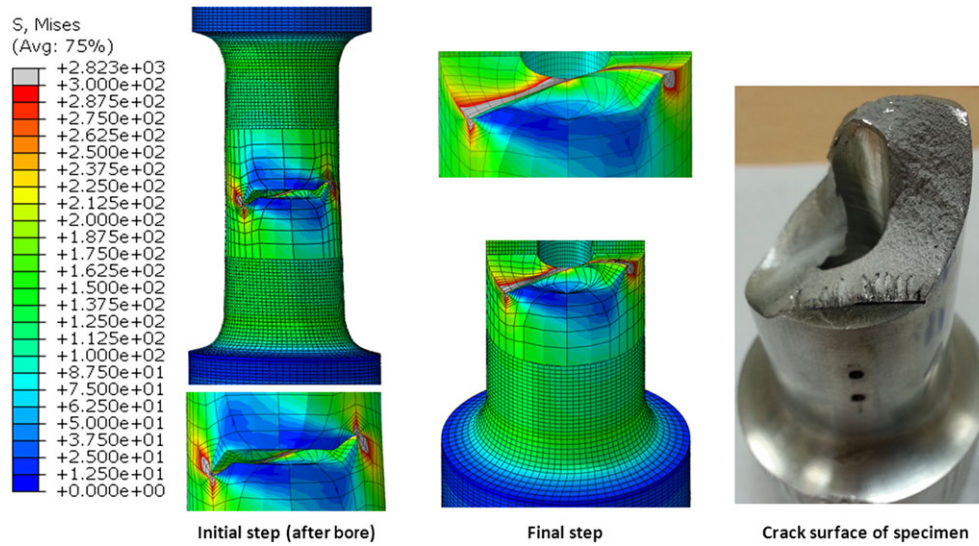


**FIGURE 11** von Mises stress scenario (MPa) for elliptical notch under axial/torsion loading at different step of crack propagation [Colour figure can be viewed at wileyonlinelibrary.com]

**TABLE 4** Comparison of numerical and experimental results

Notch Shape	Loading Condition	Number of Cycles to Reach the Bore		Number of Cycles to Final Failure	
		Exp.	Num.	Exp.	Num.
Elliptical	Axial	274 210	287 949	323 323	318 149
Elliptical	Axial/torsion	---	77 894	82 500	80 245



experimental tests).  $K_{eff}$  is an effective SIF, calculated from the mode I, mode II, and mode III  $K$  values, as shown in the following. The crack propagation was simulated under constant amplitude load and stress ratio  $R = 0.1$ .

The strain energy release rate, obtained from the J-integral calculated by the FE solver, was used to drive crack growth calculations. The maximum energy release rate criterion was adopted to calculate the crack path.

There are several approaches to calculate SIFs such as crack tip opening displacement (CTOD) approach,<sup>27,28</sup> crack tip stress field approach,<sup>29</sup> SIF extraction method from J-integral,<sup>13,22</sup> averaged strain energy density (SED) approach,<sup>30</sup> and peak stress method (PSM).<sup>31,32</sup> In

the present work, the SIFs are extracted from the J-integral based on the following equation:

$$J = \frac{B}{E} \cdot (K_I^2 + K_{II}^2) + \frac{1}{2G} \cdot K_{III}^2, \quad (2)$$

where  $B = (1 - \nu^2)$  for plane strain and 1 for plane stress and  $G$  is the tangential modulus of elasticity.

The  $K_{eff}$  is calculated as in the following formula:

$$K_{eff} = \left( \frac{B}{E} \cdot (K_I^2 + K_{II}^2) + \frac{1 + \nu}{B} \cdot K_{III}^2 \right)^{1/2}. \quad (3)$$

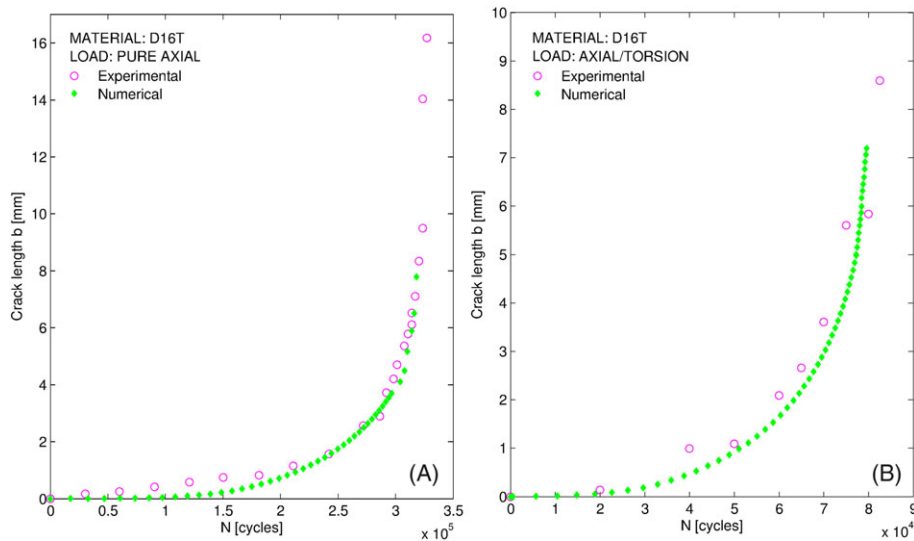


**FIGURE 12** Arc crack length  $b$  vs cycle curve for specimens with elliptical notch: under axial load A, and axial/torsion loading B, [Colour figure can be viewed at [wileyonlinelibrary.com](#)]

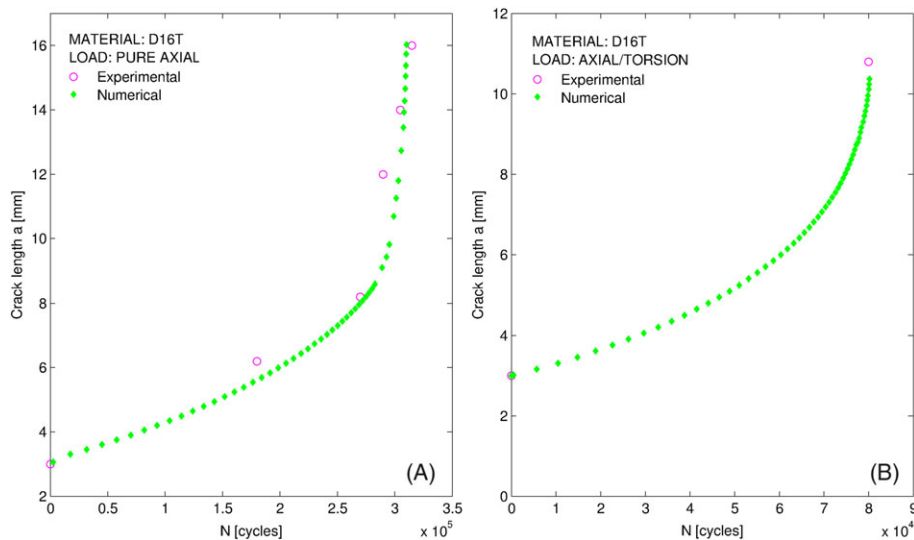


**FIGURE 13** Crack depth  $a$  vs cycle curve for specimen with elliptical notch: under axial load A, and axial/torsion loading B, [Colour figure can be viewed at [wileyonlinelibrary.com](#)]

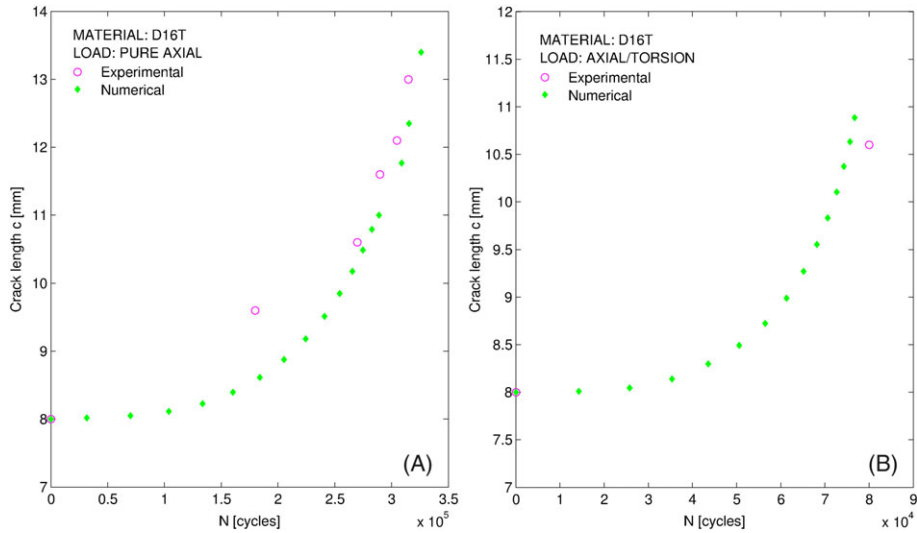


**FIGURE 14** Crack cord  $c$  vs cycle curve for specimens with elliptical notch: under axial load A, and axial/torsion loading B, [Colour figure can be viewed at wileyonlinelibrary.com]

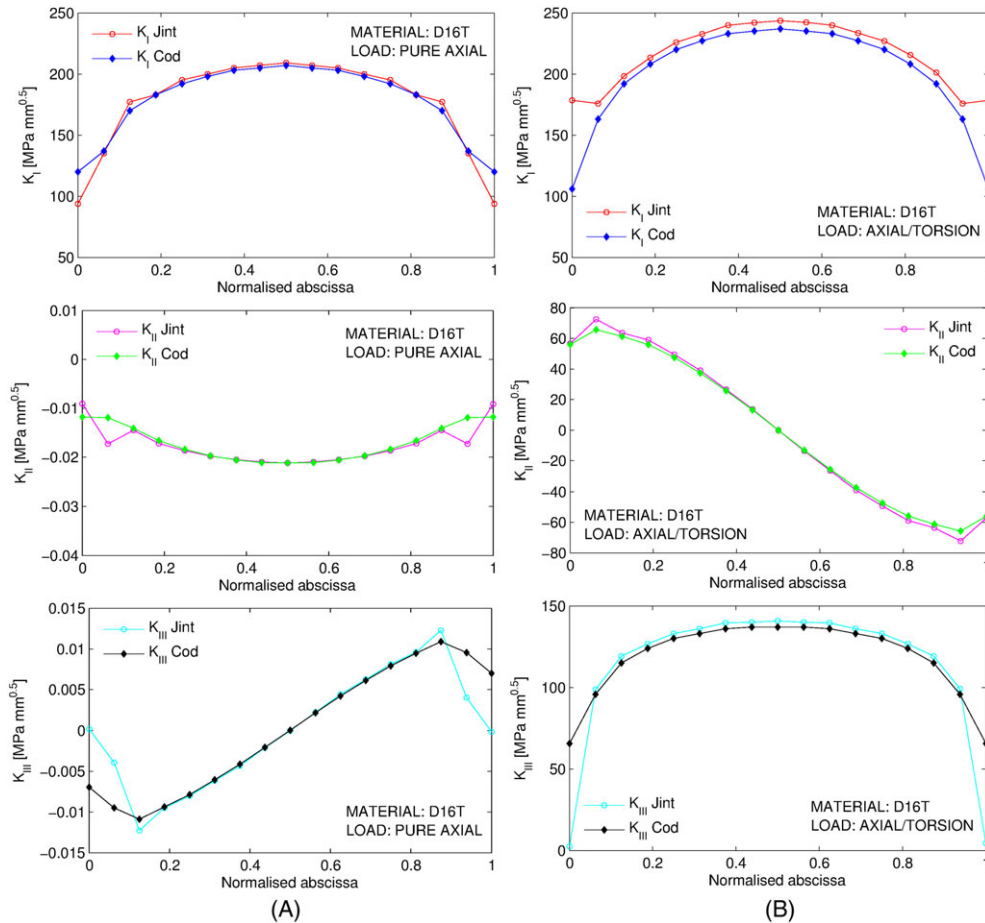


**FIGURE 15** SIFs ( $\text{MPa mm}^{0.5}$ ) along the crack front, as calculated by J-integral and COD approaches, for mode I ( $K_I$ ), mode II ( $K_{II}$ ), and mode III ( $K_{III}$ ) at step (0): specimen under pure tension loading A, and specimen under axial/torsion loading B, [Colour figure can be viewed at wileyonlinelibrary.com]

The crack propagation was simulated in two subsequent steps:

1. The first starting from the initial crack configuration up to the configuration in which the crack reaches the bore.
2. The second starting with two (wall-through) crack fronts and ending with the final failure.

## 5 | NUMERICAL RESULTS

- Axial loading

The simulated crack propagation, from the initial crack up to the final scenario, is depicted in Figure 9: the numerical simulation starts after the precracking phase, with an initial crack corresponding to the first recorded crack front, after  $N_0 = 30\,177$  cycles.

- Combined axial/torsional loading

Figure 10 shows the crack propagation for the specimen under axial/torsion loading, starting from the initial configuration (step 0) up to the intermediate step when the crack reaches the bore. The numerical simulation starts after the precracking phase, with an initial crack corresponding to the first recorded crack front, after  $N_0 = 50\,000$  cycles. Figure 11 shows crack propagation from the aforementioned intermediate step up to failure.

In Figure 11, the crack kinking induced by the mode II and III superposition, coming from the torsion load, is evident. A qualitative comparison between the numerical and experimental crack shape shows a satisfactory agreement (Figure 11).

In Table 4, numerical and experimental results are shown, with reference to the number of cycles needed for the crack to reach the bore and from bore to final failure. A satisfactory agreement is displayed.

In Figures 12–14, it is possible to appreciate the good level of correlation between experimental and numerical crack growth geometric parameters for both the analysed specimens.

$K_I$ ,  $K_{II}$ , and  $K_{III}$  values along crack front for the initial step (0), in the case of pure axial load, are plotted in Figure 15A: The crack propagates under pure mode I conditions because  $K_{II}$  and  $K_{III}$  values are negligible. Figure 15B shows  $K_I$ ,  $K_{II}$ , and  $K_{III}$  values along crack front at initial steps (0) for axial-torsion loading condition: due to the presence of torsion loading (mode III), also mode II crack conditions are generated along the initial crack front with relatively high  $K_{II}$  values.<sup>13,22</sup> This problem was widely discussed in Pook et al.<sup>33,34</sup> The authors proved that modes II and III at the crack tip cannot exist

in isolation. Mode II causes mode III, and mode III generates mode II, and these induced modes are properly named coupled modes.

## 6 | CONCLUSIONS

In this study, fatigue surface crack growth rates for D16T (2024) and B95AT (7075) aluminium alloys were determined experimentally and numerically. The crack growth rates (considering the same loading conditions) for the specimens with circular and elliptical notch in B95AT are higher than those related to specimen D16T. In the case of elliptical notch, superimposed in-phase torsion and axial loading conditions lead to an increase of crack growth rates for D16T and to a decrease for B95AT specimens. It has been also found that the crack length along the outer surface direction can be correlated with *COD* for all the types of loadings and materials using a unique fitting curve, with a small scatter: This fact suggests the possibility of crack length assessment from *COD* experimental measurements.

The computed FEM crack propagation results have been compared with the corresponding experimental ones; a good agreement has been achieved in terms of crack path and crack growth rates. Moreover, a complex 3D crack growth behaviour has been observed under superimposed axial/torsion loading. Specifically, it appears that the residual fatigue life decreases when an in-phase cyclic torsion is added to the cyclic axial load. This can be put in relation to the increase of the mode mixity. The computational strategy adopted in this study allows a reduction of the crack modelling preprocessing time thanks to the fact that it can be introduced easily and the propagation simulation is fully automatic (at each step, the model is remeshed without the user intervention).

## ORCID

Raffaele Sepe  <http://orcid.org/0000-0002-1089-4541>

## REFERENCES

1. Shlyannikov VN. Fatigue shape analysis for internal surface flow in a pressurized hollow cylinder. *Int J Press Vess Pip.* 2000;77(5):227-234.
2. Sahu VK, Ray PK, Verma BB. Experimental fatigue crack growth analysis and modelling in part-through circumferentially precracked pipes under pure bending load. *Fatigue Fract Eng Mater Struct.* 2017;40(7):1154-1163.
3. Yang F, Kuang Z. Fatigue crack growth for a surface crack in a round bar under multi-axial loading condition. *Fatigue Fract Eng Mater Struct.* 2005;28(11):963-970.

4. Citarella R, Cricri G, Lepore M, Perrella M. DBEM and FEM analysis of an extrusion press fatigue failure. In: Öchsner A, da Silva LFM, Altenbach H eds. *Materials with Complex Behaviour-Advanced Structured Materials*. 2010; 3 (2): 181-191. Berlin, Germany: Springer - Verlag.
5. Giannella V, Fellingner J, Perrella M, Citarella R. Fatigue life assessment in lateral support element of a magnet for nuclear fusion experiment "Wendelstein 7-X". *Eng Fract Mech*. 2017;178:243-257.
6. Citarella R, Giannella V, Vivo E, Mazzeo M. FEM-DBEM approach for crack propagation in a low pressure aeroengine turbine vane segment. *Theor Appl Fract Mech*. 2016;86:143-152.
7. Citarella R, Giannella V, Lepore MA, Fellingner J. FEM-DBEM approach to analyse crack scenarios in a baffle cooling pipe undergoing heat flux from the plasma. *AIMS Materials Science*. 2017;4(2):391-412.
8. Fellingner J, Citarella R, Giannella V, et al. Overview of fatigue life assessment of baffles in Wendelstein 7-X. *Fusion Eng Des*. 2018. <https://doi.org/10.1016/j.fusengdes.2018.02.011>
9. Carpinteri A, Brighenti R, Spagnoli A. Fatigue growth simulation of part-through flaws in thick walled pipes under rotary bending. *Int J Fatigue*. 2000;22(1):1-9.
10. Carpinteri A, Brighenti R. Circumferential surface flaws in pipes under cyclic axial loading. *Eng Fract Mech*. 1998;60(4):383-396.
11. Predan J, Mocišnik V, Gubelj N. Stress intensity factors for circumferential semielliptical surface cracks in a hollow cylinder subjected to pure torsion. *Eng Fract Mech*. 2013;105:152-168.
12. Giannella V, Perrella M, Citarella R. Efficient FEM-DBEM coupled approach for crack propagation simulations. *Theor Appl Fract Mech*. 2017;91:76-85.
13. Citarella R, Buchholz FG. Comparison of crack growth simulation by DBEM and FEM for SEN-specimens undergoing torsion or bending loading. *Eng Fract Mech*. 2008;75(3-4):489-509.
14. Citarella R, Lepore M, Maligno A, Shlyannikov V. FEM simulation of a crack propagation in a round bar under combined tension and torsion fatigue loading. *Frattura Ed Integrità Strutturale*. 2015;31:138-147.
15. Citarella R, Lepore M, Shlyannikov V, Yarullin R. Fatigue surface crack growth in cylindrical specimen under combined loading. *Eng Fract Mech*. 2014;131:439-453.
16. Citarella R, Giannella V, Lepore M, Dhondt G. Dual boundary element method and finite element method for mixed-mode crack propagation simulations in a cracked hollow shaft. *Fatigue Fract Eng Mater Struct*. 2018;41(1):84-98.
17. Shahani AR, Habibi SE. Stress intensity factors in a hollow cylinder containing a circumferential semi-elliptical crack subjected to combine loading. *Int J Fatigue*. 2007;29(1):128-140.
18. Schöllmann M, Fulland M, Richard HA. Development of a new software for adaptive crack growth simulations in 3D structures. *Eng Fract Mech*. 2003;70(2):249-268.
19. Carter BJ, Wawrzynek PA, Ingraffea AR. Automated 3-D crack growth simulation. *Int J Numer Methods Engng*. 2000;47(1-3): 229-253.
20. Rabold F, Kuna M. Automated finite element simulation of fatigue crack growth in three-dimensional structures with the software system ProCrack. *Proc Mater Sci*. 2014;3:1099-1104.
21. Bremberg D, Dhondt G. Automatic 3-D crack propagation calculations: a pure hexahedral element approach versus a combined element approach. *Int J Fract*. 2009;157(1-2):109-118.
22. Citarella R, Cricri G. Comparison of DBEM and FEM crack path predictions in a notched shaft under torsion. *Eng. Fract. Mech*. 2010;77(11):1730-1749.
23. Citarella R, Sepe R, Giannella V, Ishtyryakov I. Multiaxial fatigue crack propagation of an edge crack in a cylindrical specimen undergoing combined tension-torsion loading. *Procedia Struct Integrity*. 2016;2:2706-2717.
24. Zencrack 7.9-3 2015. Zentech International Limited, UK.
25. Maligno AR, Rajaratnam S, Leen SB, Williams EJ. A three-dimensional (3D) numerical study of fatigue crack growth using remeshing techniques. *Eng Fract Mech*. 2010;77(1):94-111.
26. Dassault Systems Simulia Corp. *Abaqus Analysis User's Manual, Version 6.12.1*. USA: Providence, RI; 2011.
27. Cali C, Citarella R, Perrella M. Three-dimensional crack growth: numerical evaluations and experimental tests. In: Carpinteri A, de Freitas M, Spagnoli A, eds. *Biaxial/Multiaxial Fatigue and Fracture*. Vol.31. Elsevier, Oxford, UK: European Structural Integrity Society; 2003:3-504.
28. Citarella R, Perrella M. Multiple surface crack propagation: numerical simulations and experimental tests. *Fatigue Fract Eng Mater Struct*. 2005;28(1-2):135-148.
29. Dhondt G. Application of the finite element method to mixed-mode cyclic crack propagation calculations in specimens. *Int J Fatigue*. 2014;58:2-11.
30. Lazzarin P, Berto F, Zappalorto M. Rapid calculations of notch stress intensity factors based on averaged strain energy density from coarse meshes: theoretical bases and applications. *Int J Fatigue*. 2010;32(10):1559-1567.
31. Meneghetti G, Lazzarin P. Significance of the elastic peak stress evaluated by FE analyses at the point of singularity of sharp V-notched components. *Fatigue Fract Eng Mater Struct*. 2007;30(2):95-106.
32. Meneghetti G, Campagnolo A, Avalle M, et al. Rapid evaluation of notch stress intensity factors using the peak stress method: comparison of commercial finite element codes for a range of mesh patterns. *Fatigue Fract Eng Mater Struct*. 2018;41(5):1044-1063.
33. Pook LP, Berto F, Campagnolo A. State of the art of corner point singularities under in-plane and out-of-plane loading. *Eng Fract Mech*. 2017;174:2-9.
34. Pook LP, Campagnolo A, Berto F. Coupled fracture modes of discs and plates under anti-plane loading and a disc under in-plane shear loading. *Fatigue Fract Eng Mater Struct*. 2016;39(8): 924-938.

**How to cite this article:** Lepore MA, Yarullin R, Maligno AR, Sepe R. A computational strategy for damage-tolerant design of hollow shafts under mixed-mode loading condition. *Fatigue Fract Eng Mater Struct*. 2018;1-12. <https://doi.org/10.1111/ffe.12934>